Supplement of Atmos. Chem. Phys., 21, 12243–12260, 2021
https://doi.org/10.5194/acp-21-12243-2021-supplement

Supplement of

Kinetics and impacting factors of HO_2 uptake onto submicron atmospheric aerosols during the 2019 Air QUAlity Study (AQUAS) in Yokohama, Japan

Jun Zhou et al.

Correspondence to: Jun Zhou (junzhou@jnu.edu.cn) and Yoshizumi Kajii (kajii.yoshizumi.7e@kyoto-u.ac.jp)

The Supporting Information includes the following contents and Figures.

Contents

Air mass directions iv

Measurement strategy vii

A technique combined laser-flash photolysis with laser-induced fluorescence (LFP–LIF) viii

The enrichment of the ambient aerosols ix

HO_2 reactivity of ambient air x

Correction of gas-phase diffusion for HO_2 uptake coefficient xii

HO_2 reactivity of ambient gas phase (k_g) xiii

Temperature and pressure influence correction xiv

Profiles of key factors used in Section 3.5: xix

References xxii

Figures

Figure S1: NOAA-HYSPLIT model showing back trajectories for ~ 11 days sample periods from 12:00 July 24 to 00:00 August 04, 2019 (back trajectories ending 00:00 UTC 25 July to 00:00 August 04, 2019) from the sampling site. Arriving air masses 250 m, 500 m, and 1000 m above ground level (AGL) were calculated using the following website: http://ready.arl.noaa.gov/hypub-bin/trajtype.pl?runtype=archive vi

Figure S2: (a) Sampling setup for testing HO_2 reactivity using laser-flash photolysis and laser-induced fluorescence (LFP–LIF) with a versatile aerosol concentration enrichment system (VACES) and auto-switching aerosol filter (SMPS = scanning mobility particle sizer; AMS = aerosol mass spectrometer; CAPS=cavity attenuated phase shift). (b) Detailed presentation of the measurement process of the HO_2 reactivity of the ambient aerosol phase. Further details concerning the measurement process can be found in our previous publication[3]........ viii

Figure S3: Examples of the measured HO_2 decay profiles in zero air (black lines), ambient air without aerosol phase (green lines), and ambient air with enriched aerosol phase (red lines) at an RH of ~60%, 301 K, and an initial HO_2 concentration of ~10^{10} molecules cm^{-3}. The log scale plot in the inserted figure at the upper right shows linear fitting in the range 0.08–0.4...xii

Figure S4: Average of HO_2 reactivity calibrations using LFP–LIF with different NO_2 concentrations supplied by NO_2 gas. The green lines represent the ±68.3% prediction band of the calibration data points ($1\sigma = 0.1\ s^{-1}$), i.e., the uncertainty in the estimation of HO_2 reactivity using the calibration curve. ……………………………………………………………………………………….…...xiii

Figure S5: Diurnal trends in non-refractory chemical components plus eBC of group i (left side) and group ii (right side)……………………………………………………………………………….....xv

Figure S6: Diurnal trends in total HO_2 reactivity caused by the ambient aerosol phase (k_a, upper panel) and the HO_2 uptake coefficients onto ambient aerosols (γ, lower panel)………………….…………..xv

Figure S7: Correlations between measured and modeled γ with (a) $\gamma < 0.4$ and (b) $\gamma \geq 0.4$…………xvi

Figure S8: Time series of the half an hour averaged ambient RH (red open cycles in the upper panel) and temperature (red filled cycles in the lower panel) measurements in comparison to the reaction cell RH (black open cycles in the upper panel) and temperature (black filled cycles in the lower panel)...xvi

Figure S9: k_a and γ values as a function of RH in the reaction cell, colored coded with T……………xvii

Figure S10: k_a (upper panel) and γ (lower panel) as a function of mean particle diameter, color coded with the surface area concentration. …………………..…………………………………………………xvii

Figure S11: Dependence of day time LN/Q and LN/Q_without_aerosol on [NO]……………...…..xix

Figure S12: Temporal variations in key factors in ambient air for determining XO_2 loss rates and $P(O_3)$ sensitivity in Sect. 3.6. ……………………………………………………………………...………...xix

Tables

Table S1: Summary of equations and values used in section 3.4...xviiii

Table S2: Summary of equations and values used in section 3.6.. xvii

Air mass directions

Figure S1a shows air mass direction schematic diagram during the campaign. For each day, the Internet-Based HYSPLIT Trajectory Model and gridded meteorological data (Global Data Assimilation System, GDAS1) from the U.S. National Oceanic and Atmospheric Administration (NOAA) were used during the modeling, the tested results of all experimental days are listed in Fig. S1b. Backward trajectories ended at local time 00:00 am and 12:00 pm after a total run time of 12 h. Results suggesting that arriving air mass can be classified into two categories (i) from the sea to the north direction towards Yokohama City (~19% of the experimental period: from 12:00 pm Jul. 25 to 12:00 Jul. 27, 2019); (ii) from the mainland towards Yokohama City (~81% of the experimental period).

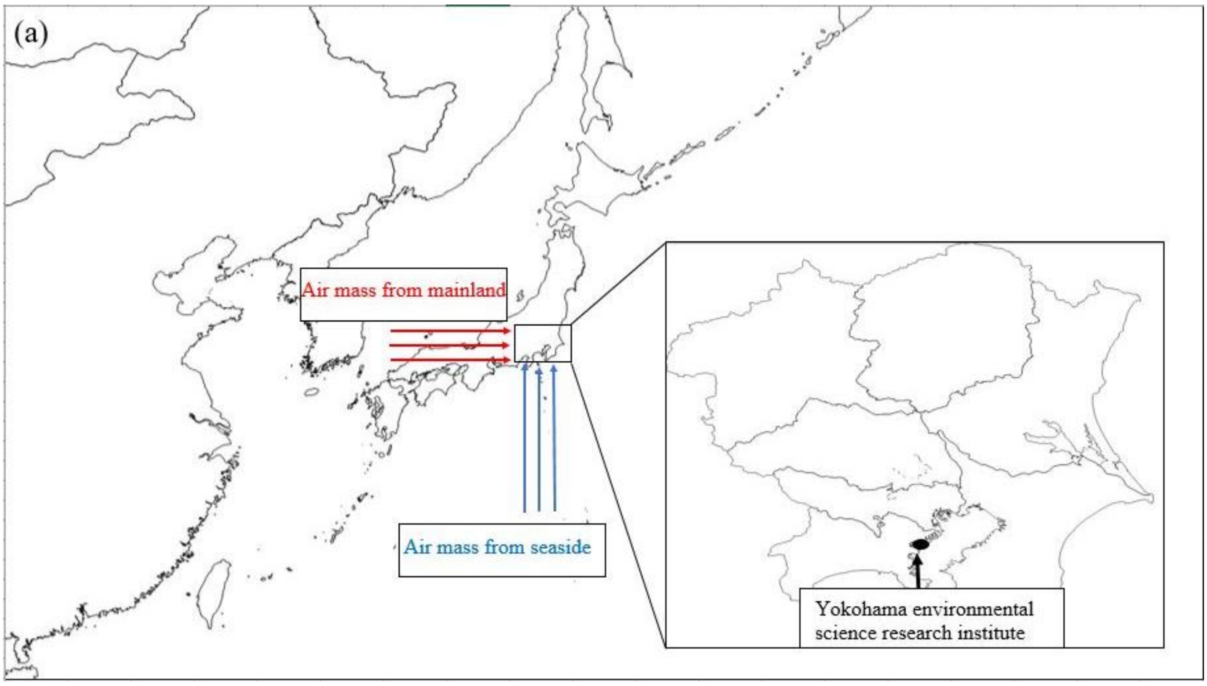

(b)

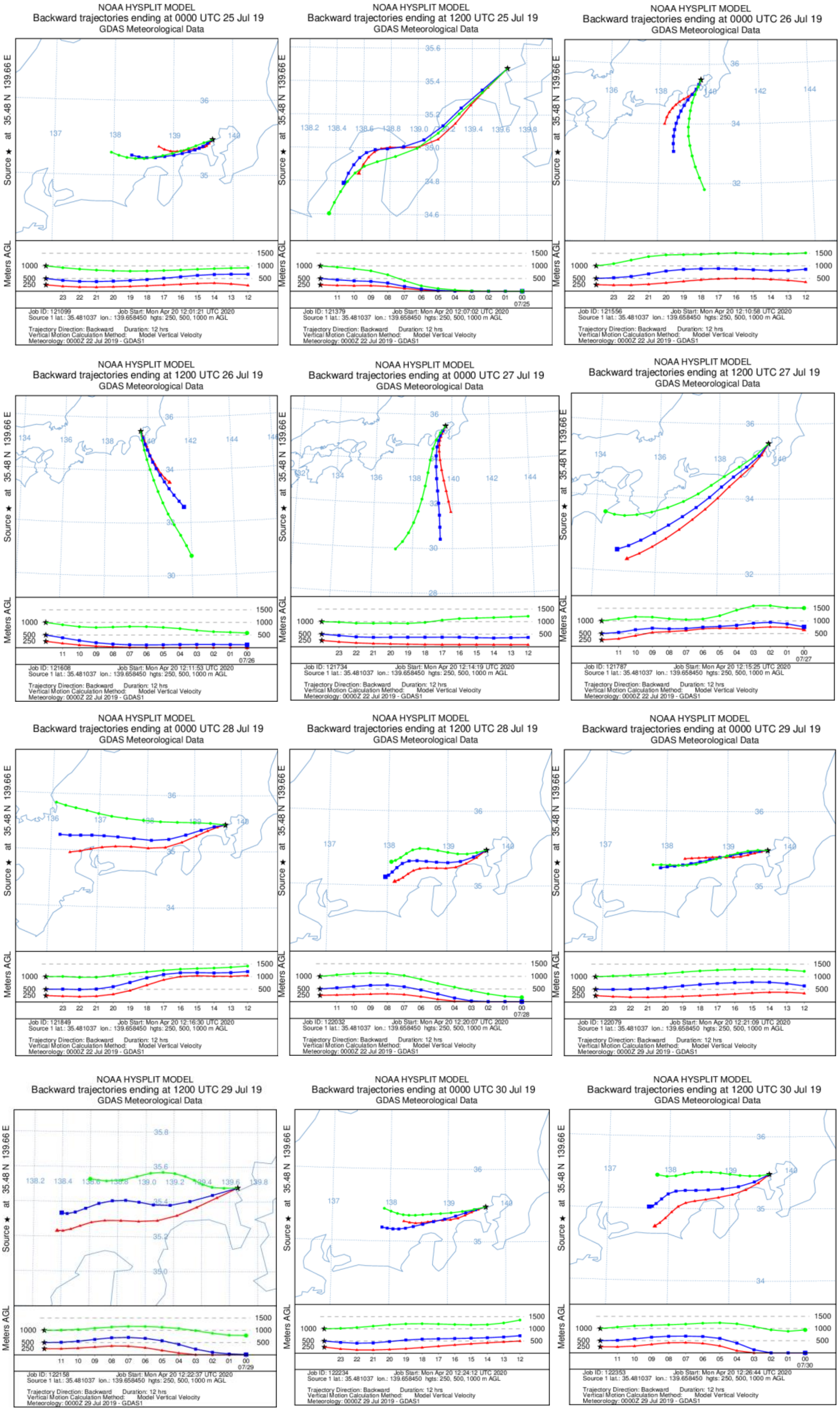
NOAA HYSPLIT MODEL
Backward trajectories ending at 0000 UTC 25 Jul 19
GDAS Meteorological Data
NOAA HYSPLIT MODEL
Backward trajectories ending at 1200 UTC 25 Jul 19
GDAS Meteorological Data
NOAA HYSPLIT MODEL
Backward trajectories ending at 0000 UTC 26 Jul 19
GDAS Meteorological Data
NOAA HYSPLIT MODEL
Backward trajectories ending at 1200 UTC 26 Jul 19
GDAS Meteorological Data
NOAA HYSPLIT MODEL
Backward trajectories ending at 0000 UTC 27 Jul 19
GDAS Meteorological Data
NOAA HYSPLIT MODEL
Backward trajectories ending at 1200 UTC 27 Jul 19
GDAS Meteorological Data
NOAA HYSPLIT MODEL
Backward trajectories ending at 0000 UTC 28 Jul 19
GDAS Meteorological Data
NOAA HYSPLIT MODEL
Backward trajectories ending at 1200 UTC 28 Jul 19
GDAS Meteorological Data
NOAA HYSPLIT MODEL
Backward trajectories ending at 0000 UTC 29 Jul 19
GDAS Meteorological Data
NOAA HYSPLIT MODEL
Backward trajectories ending at 1200 UTC 29 Jul 19
GDAS Meteorological Data
NOAA HYSPLIT MODEL
Backward trajectories ending at 0000 UTC 30 Jul 19
GDAS Meteorological Data
NOAA HYSPLIT MODEL
Backward trajectories ending at 1200 UTC 30 Jul 19
GDAS Meteorological Data
Source ★ at 35.48 N 139.66 E
Meters AGL
1500
1000
500
250

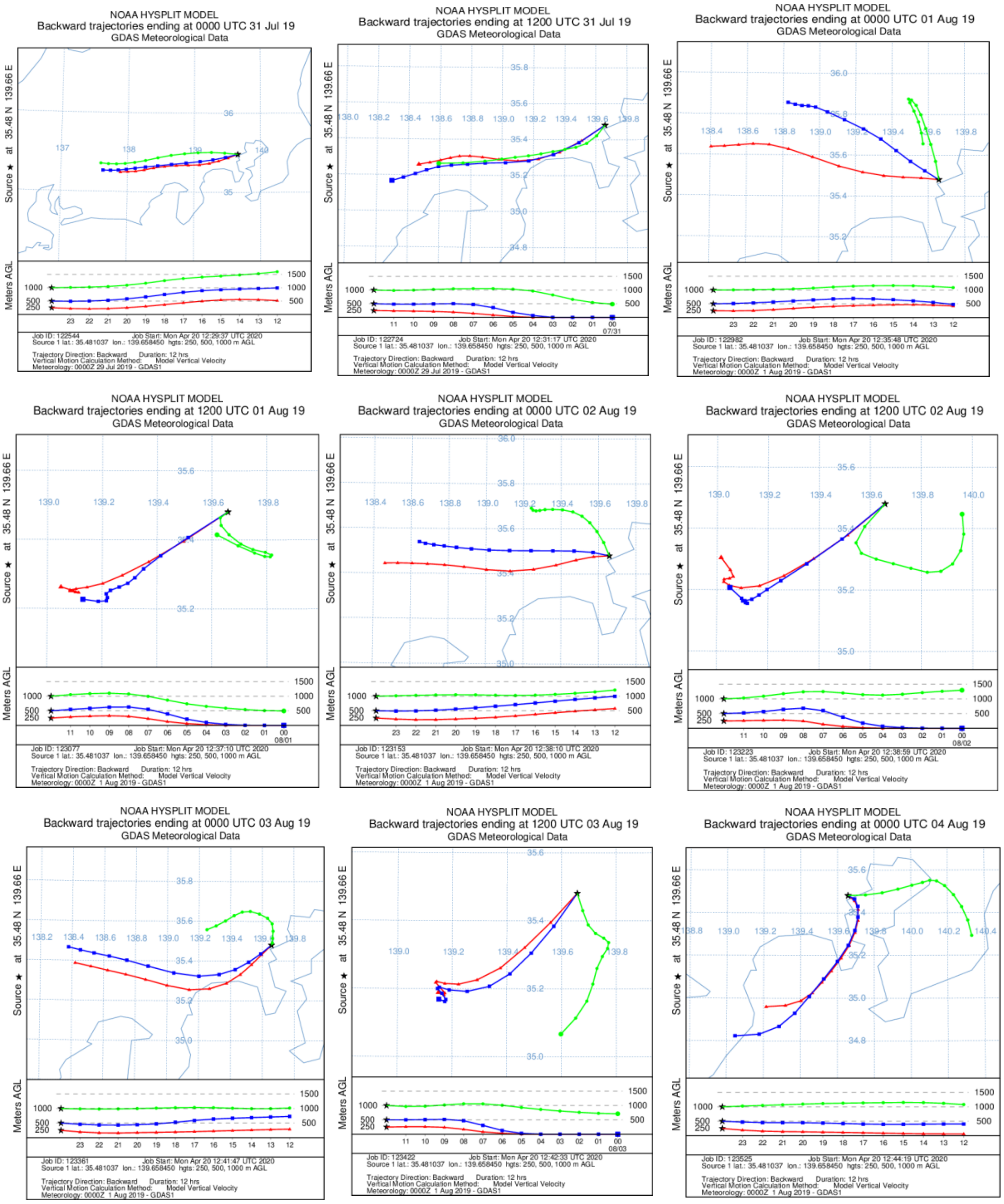

NOAA HYSPLIT MODEL
Backward trajectories ending at 0000 UTC 31 Jul 19
GDAS Meteorological Data

NOAA HYSPLIT MODEL
Backward trajectories ending at 1200 UTC 31 Jul 19
GDAS Meteorological Data

NOAA HYSPLIT MODEL
Backward trajectories ending at 0000 UTC 01 Aug 19
GDAS Meteorological Data

NOAA HYSPLIT MODEL
Backward trajectories ending at 1200 UTC 01 Aug 19
GDAS Meteorological Data

NOAA HYSPLIT MODEL
Backward trajectories ending at 0000 UTC 02 Aug 19
GDAS Meteorological Data

NOAA HYSPLIT MODEL
Backward trajectories ending at 1200 UTC 02 Aug 19
GDAS Meteorological Data

NOAA HYSPLIT MODEL
Backward trajectories ending at 0000 UTC 03 Aug 19
GDAS Meteorological Data

NOAA HYSPLIT MODEL
Backward trajectories ending at 1200 UTC 03 Aug 19
GDAS Meteorological Data

NOAA HYSPLIT MODEL
Backward trajectories ending at 0000 UTC 04 Aug 19
GDAS Meteorological Data

Figure S1: (a) Air mass direction schematic diagram; (b) NOAA-HYSPLIT model showing back trajectories for ~ 11 days sample periods from 12:00 July 24 to 00:00 August 04, 2019 (back trajectories ending 00:00 UTC 25 July to 00:00 August 04, 2019) from the sampling site. Arriving air masses 250 m, 500 m, and 1000 m above ground level (AGL) were calculated using the following website: http://ready.arl.noaa.gov/hypub-bin/trajtype.pl?runtype=archive

Measurement strategy

The HO_2 reactivity was measured using LFP–LIF, adapted from a laser-induced pump and probe OH reactivity measurement technique, which has been validated and employed for the total gas phase HOx (=OH+HO_2) reactivity and HOx uptake kinetics onto ambient aerosols in field [1, 2-4]. We further coupled this system with a versatile aerosol concentration enrichment system (VACES) to enrich the ambient aerosols to compensate the relatively low limit of detection (LOD) for the HO_2 reactivity measurement. A schematic of the experimental system is shown in Fig. S2a, and a detailed abstract of the measurement process of the HO_2 reactivity of the ambient aerosol phase is shown in Fig. S2b. The ambient air was drawn into the VACES, where the aerosol concentration was enriched. The ambient air was then sampled using a three-port valve (Bolt, Flon Industry Co., LTD) and injected into the LFP–LIF system at a flow rate of 8 L min^{-1}. The valve was switched automatically between two sampling lines, one with the aerosol filter and the other without the aerosol filter (termed “the auto-switching aerosol filter” hereafter), which enabled alternative measurements of HO_2 reactivity by the gas phase and the gas + enriched aerosol phase of the ambient air, separately.

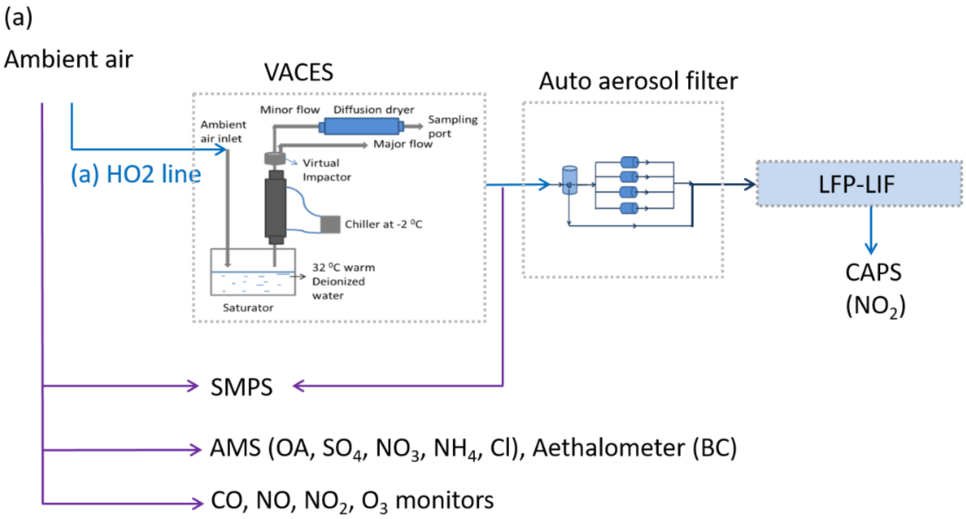

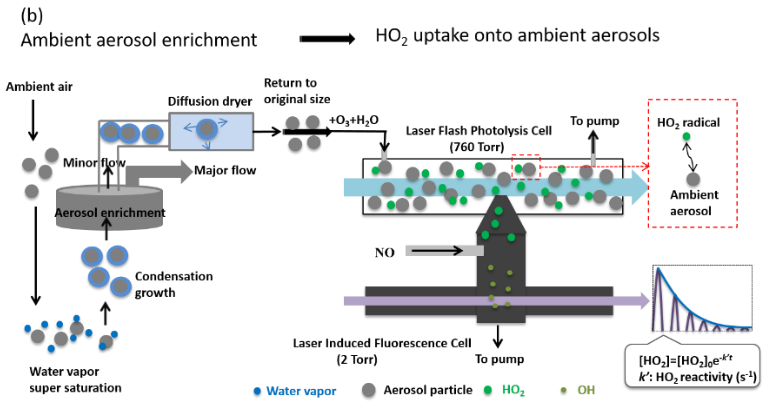

Figure S2: (a) Sampling setup for testing HO_2 reactivity using laser-flash photolysis and laser-induced fluorescence (LFP–LIF) with a versatile aerosol concentration enrichment system (VACES) and auto-switching aerosol filter (SMPS = scanning mobility particle sizer; AMS = aerosol mass spectrometer; CAPS = cavity attenuated phase shift); and (b) Detailed presentation of the measurement process of the HO_2 reactivity of the ambient aerosol phase. Further details concerning the measurement process can be found in our previous publication[3].

A technique combined laser-flash photolysis with laser-induced fluorescence (LFP–LIF)

LFP–LIF comprises two cells: the laser-flash photolysis cell (the reaction cell) and the laser-induced fluorescence detection cell (the detection cell). In the HO_2 reaction cell, pure air was supplied by a zero-air generator (Model 111, Thermo Fisher Scientific Inc., USA), and relative humidity was controlled by bubbling water vapor into one part of the zero air. The ambient air was sampled into the reaction cell after mixed with the humidified zero air and O_3, where O_3 (~100 ppb) was generated by184.9 nm irradiation of zero air by a low-pressure Hg lamp (pen ray lamp, Sen lights corporation, JP, part number: SP-5-2H (5w)) at 50 sccm (standard cubic centimeter per minute, at 273 K and 1 atm). The reaction cell was made of aluminum, with a length of 1.4 m and an inner diameter of 0.04 m, and the inner wall of the flow tube was coated with Teflon to reduce the heterogeneous losses of HO_2 and the reactants. The sample inlet of the detection cell was located ~0.7 m from the sample injection position. The total flow inside the reaction cell was ~10 L min^{-1}, with a residence time of ~4.8 s. The Reynolds number in the reaction cell was ~354 and (1 atm pressure and 298 K were assumed inside the reaction cell), thus indicating a laminar flow. A pulsed 266-nm Nd:YAG laser (Tempest 300, New Wave Research Inc., USA), with a 1-cm diameter, laser power ranging between 0.4 and 3.0 *mJ* pulse^{-1}, and a repetition of 1 Hz, was used in the reaction cell to irradiate the sample air to produce OH through reactions SR1–SR2.

$$O_3 + hv(266\ nm) \rightarrow O(^1D) + O_2 \quad (SR1)$$

$$O(^1D) + H_2O \rightarrow 2OH \quad (SR2)$$

Meanwhile, excess CO was introduced into the reaction cell to convert all OH radicals to HO_2:

$$OH + CO \rightarrow H + CO_2 \quad (SR3)$$

$$H + O_2 \rightarrow HO_2 \quad (SR4)$$

The initial HO_2 concentration in the reaction cell was of the order of 10^{10} molecules cm^{-3}, estimated from the photolysis power, humidity, and O_3 concentration[3]. A stream of flow (~ 2 LPM) in the reaction cell was pumped into the detection cell using a rotary oil pump (D-950, ULVAC) under a pressure of 1.6 Torr through a 0.5-mm pinhole. NO (>99.999%) was injected with a flow rate of 3 sccm between the reaction cell and the detection cell to convert HO_2 to OH (Eq. SR5, conversion efficiency: ~ 30%). The second harmonic of a pulsed laser (Sirah Credo, Spectra Physics) pumped by the second harmonic of a Nd:YVO4 laser (YHP40-532Q, Spectra Physics) and set at a maximum absorption of $Q_1(2)$ $A^2\Sigma^+(v' = 0) \leftarrow X^2\Pi_{3/2}(v'' = 0)$ transition of OH at 308 nm was used to irradiate the detection cell with a repetition rate of 10 kHz. The fluorescence emitted by the OH radical induced by each irradiation was collected by a photomultiplier tube (R2256P, Hamamatsu Photonics), and a decay file of OH was obtained after 240 integrations. The HO_2 decay rate was considered the same as the OH decay rate as we were measuring the relative change in the HO_2 concentration in the detection cell.

$$HO_2 + NO \rightarrow OH + NO_2 \quad (SR5)$$

The enrichment of the ambient aerosols

The versatile aerosol concentration enrichment system (VACES) was built according to Sioutas et al. (1999)[5], which comprises the aerosol growth part and the aerosol enrichment part (as shown in Fig. S2a). The ambient air sample was drawn into VACES at a flow rate of over 100 L min^{-1} (Q_{tot}) into a ultra-pure water tank which was heated to ~32°C, where the ambient air steam was saturated and then cooled down in a condenser connected immediately above the tank (with a temperature of −2 °C). The growed ambient aerosol (mostly with a diameter > 2 μm) through condensed water droplets were then enriched by a virtual impactor with a 50% cutoff point less than 1 μm, with ~92 L min^{-1} going to the major flow that connected to the exhaust pump and ~8 L min^{-1} going to the minor flow (q_{min}) that connected to the aerosol instrumentations after passing through a diffusion dryer. In theory, the enrichment factor (EF) of the ambient aerosol concentration can be estimated as:

$$EF = Q_{tot}/q_{min}(1 - WL) \times \eta_{vi} \tag{S1}$$

where η_{vi} and WL are its collection efficiency and fractional loss, respectively[5]. The enrichment efficiency (EE) of the impactor was estimated as ~ 1[3]. In this study, we test the enrichment factor of the surface area of the enriched ambient aerosols (*E*) by connecting two SMPS before and after VACES separately for ~ 2 hours every day for ~ 6 days, the enrichment factor can be calculated as:

$$E = S_1/S_2 \tag{S2}$$

Where S_1 and S_2 are the surface areas of the enriched ambient aerosols after VACES and the ambient aerosols before VACES, respectively. Obtained *E* values from all the tests were then averaged and used as the final enrichment factor (~ 12.5±2.5) for all the experimental days. The surface area of the enriched ambient aerosols with diameters < 2.5 μm (*E*S) are propagated from S_1 multiply the ratio between mass concentration of $PM_{2.5}$ and $PM_{0.74}$ (calculated as ~1.1), by assuming the total volume and the total surface area of each size distribution bin (ranged from 0 to 2.5 μm) of $PM_{2.5}$ are increased in proportional with mass concentration compared to that of $PM_{0.75}$ (ranged from 0 to 0.75μm):

$$ES = \frac{PM_{2.5}}{PM_{0.74}} \times S_1 \tag{S3}$$

HO_2 reactivity of ambient air

Owing to the excess CO, almost all HO_2 radicals formed in the reaction cell after the photolysis pulse, and the HO_2 and RO_2 radicals in urban ambient air were destroyed, or at least partially, during their intake into the LFP detection cell, thus the self-reaction of HO_2 and the interaction of HO_2 with RO_2 owing to the inherent HO_2/RO_2 concentrations from ambient air was negligible. Due to the large excess reactants over HO_2 radicals produced in the LFP reaction cell, pseudo-first order conditions were achieved, and the HO_2 decay rate *k* (HO_2 reactivity) can be explained through the following equation[2]:

$$\frac{d[\mathrm{HO_2}]}{dt} = -(k_{\mathrm{NO2}}[\mathrm{NO_2}] + k_{\mathrm{NO}}[\mathrm{NO}] + k_{\mathrm{aerosol}}[\text{ambient aerosol}] + k_{\mathrm{wall}}) \times [\mathrm{HO_2}] \tag{S4}$$

where k_i is the rate constant of the HO_2 reaction with different reacting species i, where i = NO_2, NO and the ambient aerosols. k_{wall} is the loss rate of the HO_2 radicals onto the wall, and $[i]$ represents the concentration of the reacting species i. Due to the short reaction time, k_{wall} was small and included in the baseline. And the consumption of HO_2 by NO in the reaction cell is immediately compensated by excess CO, converting its product OH back to HO_2; therefore, the HO_2 decay in the LFP reaction cell may be mostly attributed to its reaction with NO_2 and aerosol phase. The reaction with NO_2 will produce peroxynitric acid:

$$\mathrm{HO_2} + \mathrm{NO_2} \overset{\mathrm{M}}{\rightarrow} \mathrm{HO_2NO_2} \tag{SR6}$$

Ideally, the thermal unimolecular decomposition of HO_2NO_2 may occur. However, we didn't consider this reverse reaction, due to (1) The reaction cell (~40 mm diameter) is considerably larger than the reaction-initialized region (the laser beam covered area, ~10 mm diameter). The HO_2, NO_2, and HO_2NO_2 that are produced will diffuse to the outside of the reaction-initialized region (~16 times diluted), thus largely reducing the reactant concentrations. Further, reproducing the reaction process is impossible because the sampling port of the defection cell is located in the center of the reaction-initialized region; (2) The log scale plot of the HO_2 decay profile as a function of time was linear in the fitting range (as illustrated in Fig. S3). 3) As shown in Fig. S4, the HO_2 reactivity exhibited a linear correlation with the wide concentration range of NO_2. These phenomena indicate the negligible influence of the reverse reaction to the gas phase HO_2 reactivity. We also observed the negligible reverse reaction previously, even in the case of lower HO_2 and NO_2 concentrations[2]. We assume the heterogeneous loss of HO_2 by the aerosol following the single first order reaction step as:

$$\mathrm{HO_2}\text{+aerosol} \rightarrow \text{no products (in gas phase)} \tag{SR7}$$

HO_2 was converted to OH in the reaction with NO in the detection cell, according to Eq. SR5. The HO_2 concentrations were then measured by laser-induced fluorescence from OH after each probe laser (266 nm) irradiation to obtain a decay curve. Examples of the time series of HO_2 decay files of zero air, ambient air without aerosols and ambient air with enriched aerosols are shown in Fig. S3.

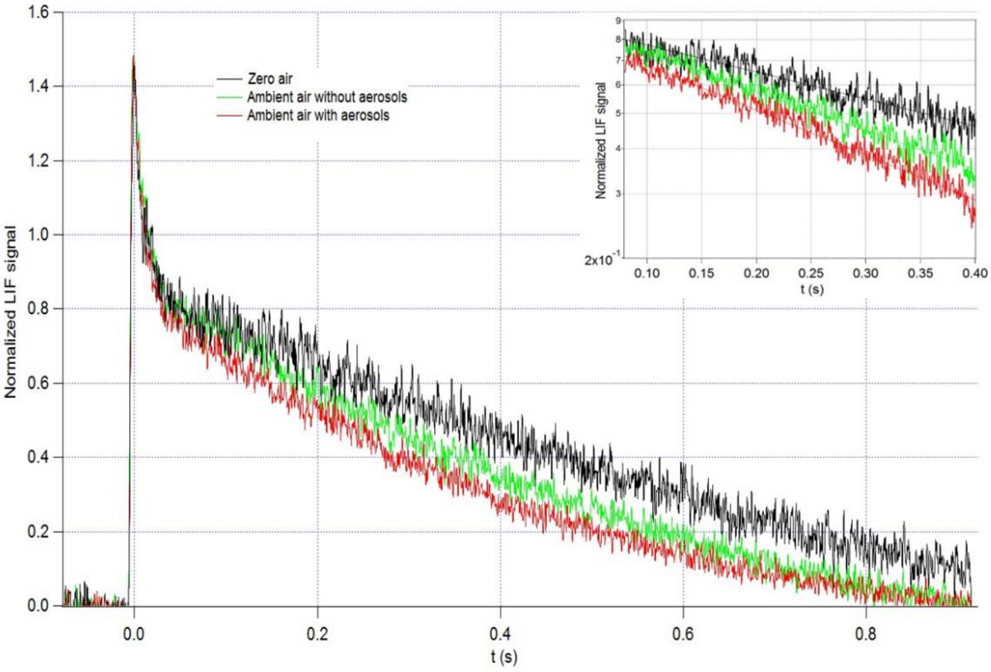

Figure S3: Examples of the measured HO_2 decay profiles in zero air (black lines), ambient air without aerosol phase (green lines), and ambient air with enriched aerosol phase (red lines) at an RH of ~60%, 301 K, and an initial HO_2 concentration of ~10^{10} molecules cm^{-3}. The log scale plot in the inserted figure at the upper right shows linear fitting in the range of 0.08–0.4.

Correction of gas-phase for HO_2 uptake coefficient

γ_{obs} includes the gas phase diffusion, and as the HO_2 radical is active in aerosol bulk, the resistance model was usually utilized for explaining the observed uptake coefficients (George et al., 2013; Davidovits et al., 2006):

$$\frac{1}{\gamma_{\text{obs}}} = \frac{1}{\gamma_{\text{diffusion}}} + \frac{1}{\alpha} + \frac{1}{\gamma_{\text{reaction+partitioning}}} \tag{S5}$$

where γ_{obs} and $\gamma_{\text{diffusion}}$ represent the observed uptake coefficients and the gas transport coefficient, respectively, α is the mass accommodation, and the third term represents the resistance caused by the sum of the reactive and partitioning processes within the aerosol. The observed uptake coefficients were further corrected to take into account gas diffusion contribution, and the final γ can be obtained from Eq. S6[6, 7]:

$$\gamma = \frac{\gamma_{\mathrm{obs}}}{1-\gamma_{\mathrm{obs}}\lambda(r_{\mathrm{s}})} \tag{S6}$$

where $\lambda(r_{\mathrm{s}})$ are is obtained from Eq. S7:

$$\lambda(r_{\mathrm{s}}) = \frac{0.75+0.283K_{\mathrm{n}}}{K_{\mathrm{n}}(1+K_{\mathrm{n}})} \tag{S7}$$

where $K_{\mathrm{n}} = \frac{3D_{\mathrm{g}}}{w_{\mathrm{HO_2}} r_{\mathrm{s}}}$ (S8)

where D_g is the gas phase diffusion coefficient of HO_2 (0.25 cm^2 s^{-1}) at ~298 K, and r_{s} represents the average radius of the aerosols, defined as follows:

$$r_{\mathrm{s}}^2 = \frac{A_{\mathrm{total}}}{4\pi N_{\mathrm{total}}} \tag{S9}$$

where A_{total} denotes the total surface area measured and N_{total} denotes the total number of particles producing that surface area.

HO_2 reactivity of ambient gas phase (k_g)

Gas phase HO_2 reactivity was directly measured in the reaction cell without aerosol phase. To check the dominant factor of the gas phase HO_2 reactivity, we modeled the HO_2 reactivity by using the NO_2 concentration in the LFP reaction cell, using the calibration factor obtained by plotting the measured HO_2 decay rates as a function of the NO_2 concentration prepared in the laboratory (with the NO_2 concentration in zero air ranging from 0 to 85 ppb at 298 K and 1 atm in the reaction cell, Fig. S4).

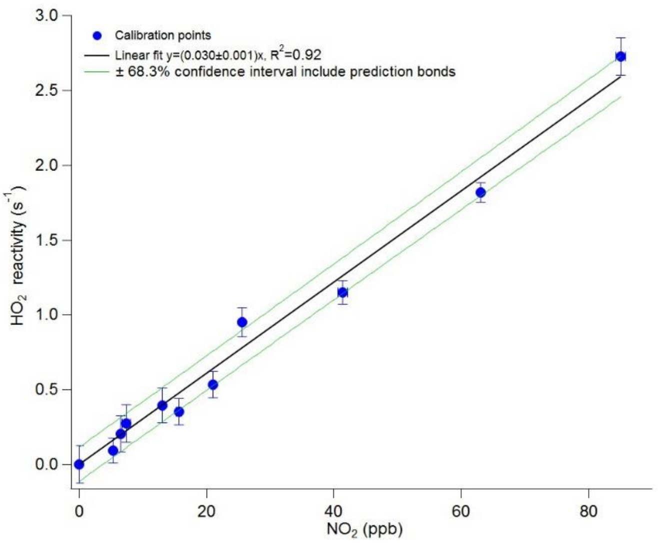

Figure S4: Average of HO_2 reactivity calibrations using LFP–LIF with different NO_2 concentrations supplied by NO_2 gas. The green lines represent the ±68.3% prediction band of the calibration data points ($1\sigma = 0.1\ s^{-1}$), i.e., the uncertainty in the estimation of HO_2 reactivity using the calibration curve.

The linear fitting coefficient represents the HO_2 reactivity with NO_2 concentrations in the reaction cell, which was 0.030 $s^{-1}\ ppb^{-1}$ with a standard deviation of 0.001. This indicates that the instrument accuracy in determining $k_{\mathrm{HO_2}}$ from NO_2 concentration was 3%. This calibration factor was used to simulate HO_2 reactivity ($k_{\mathrm{HO_2}}$) caused by NO_2 from ambient air in the LIF reaction cell as follows:

$$k_{\mathrm{HO_2}}(\mathrm{s}^{-1}) = (0.030\ (\mathrm{s}^{-1}/\mathrm{ppb}) \times \Delta\mathrm{NO_2}(\mathrm{ppb})\ ) \times (\frac{k_f([M],T)}{k_c([M],T)}) \qquad \text{(S10)}$$

where $\Delta\mathrm{NO_2}$ denotes the difference between the $\mathrm{NO_2}$ concentrations in ambient air and zero gas (here NO_2 is ~0.5 ppb in zero gas, which may be due to the interferences in zero gas), while $k_f([M],T)$ and $k_c([M],T)$ denote the rate constant calculated from the equations recommended by Sander et al. (2011)[8] using the temperature in the reaction cell at the ambient air measurement time and calibration time, respectively.

Temperature and pressure influence correction

Reaction in SR6 is favored by low-temperature and high-pressure conditions and is believed to play an important role in the free troposphere and particularly the upper troposphere as it becomes cooler with higher pressure [9]. The room temperature was maintained at 298 K during the whole campaign. However, the temperature in the reaction cell ranged from 298 K to 302 K due to the sampled ambient air temperature. The temperature and pressure correction was done according to the procedure adopted by the National Aeronautics and Space Administration (NASA) data evaluation panel, as follows[8]:

$$k_f([M],T) = \left[\frac{k_0(T)[M]}{1+\frac{k_0(T)[M]}{k_\infty(T)}}\right]0.6^{\left\{1+\left[log_{10}\left(\frac{k_0(T)[M]}{k_\infty(T)}\right)\right]^2\right\}^{-1}} \tag{S11}$$

where $k_0(T)$ denotes the low-pressure-limiting rate constants, which can be calculated as:

$$k_0(T) = k_0^{300}\left(\frac{T}{300}\right)^{-n}\ \mathrm{cm^6 molecule^{-2} s^{-1}} \tag{S12}$$

and $k_\infty(T)$ denotes the limiting high-pressure rate constant, which can be calculated similarly:

$$k_\infty(T) = k_\infty^{300}\left(\frac{T}{300}\right)^{-m}\ \mathrm{cm^3 molecule^{-1} s^{-1}} \tag{S13}$$

Here, n and m in Eqs. S11&S12 represent the temperature-dependent coefficients, which are recommended as 0.34 ± 0.4 and 1.1 ± 1.4, respectively. The equilibrium constants at temperature *T*, *K* (*T*), can be expressed as:

$$K(T) = \frac{k_f([M],T)}{k_{-1}(T)} = 2.1\times10^{-27}\left(\frac{10900}{T}\right)\ \mathrm{cm^3\ molecule^{-1}\ s^{-1}} \tag{S14}$$

Thus, $k_{-1}(T)$, which is the rate constant of the reverse reaction of SR6, can be calculated from the known *K* (*T*) and $k_f([M],T)$.

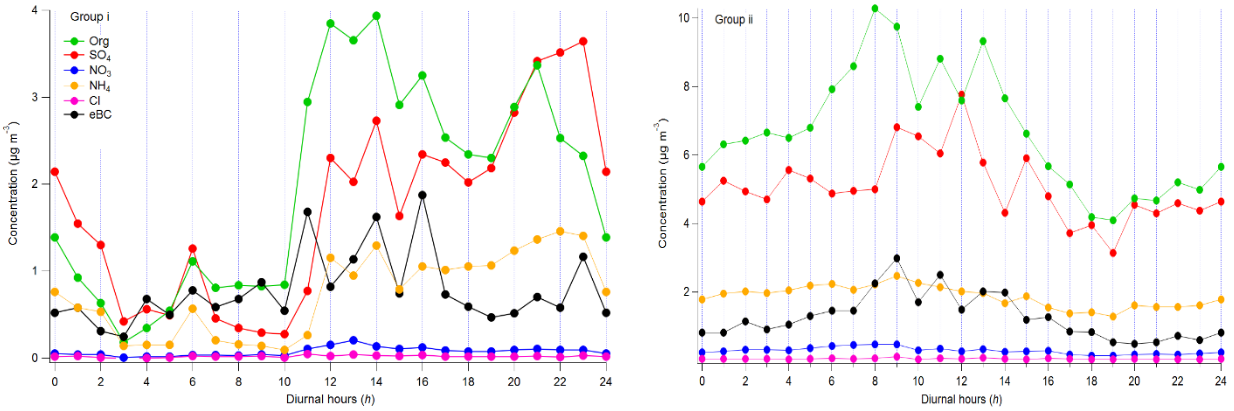

Figure S5: Diurnal trends in non-refractory chemical components plus eBC of group i (left side) and group ii (right side).

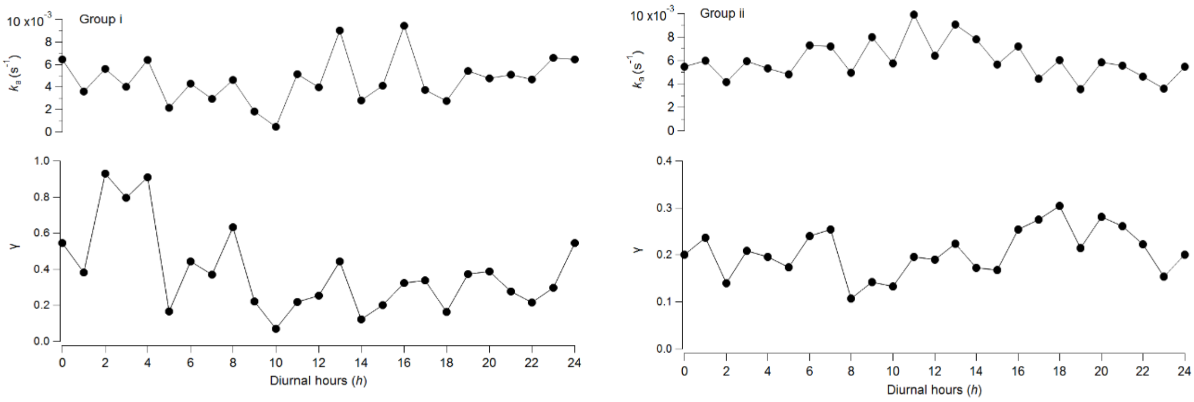

Figure S6: Diurnal trends in total HO_2 reactivity caused by the ambient aerosol phase (k_a, upper panel) and the HO_2 uptake coefficients onto ambient aerosols (γ, lower panel).

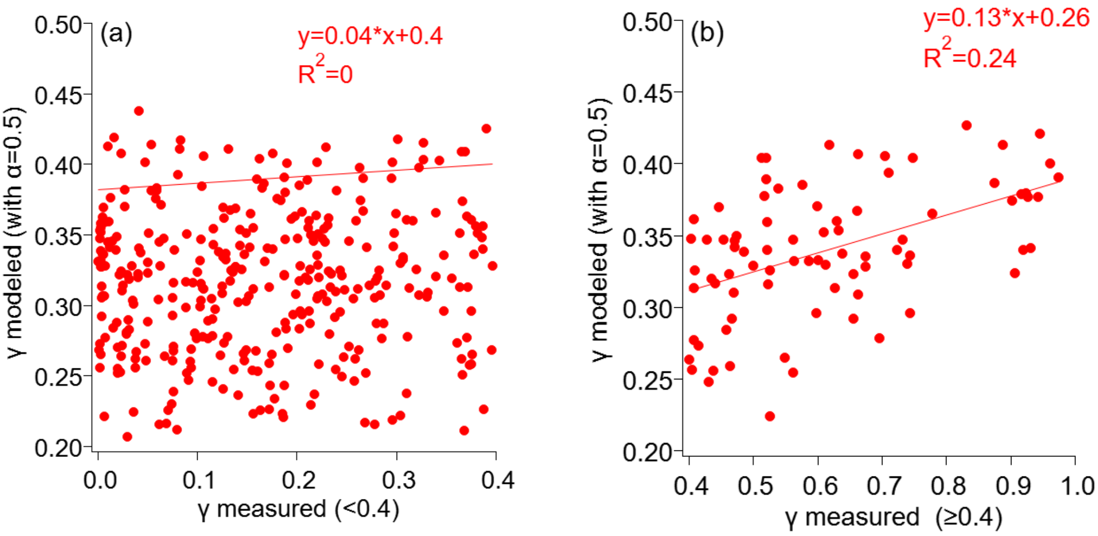

Figure S7: Correlations between measured and modeled γ with (a) $\gamma < 0.4$ and (b) $\gamma \geq 0.4$.

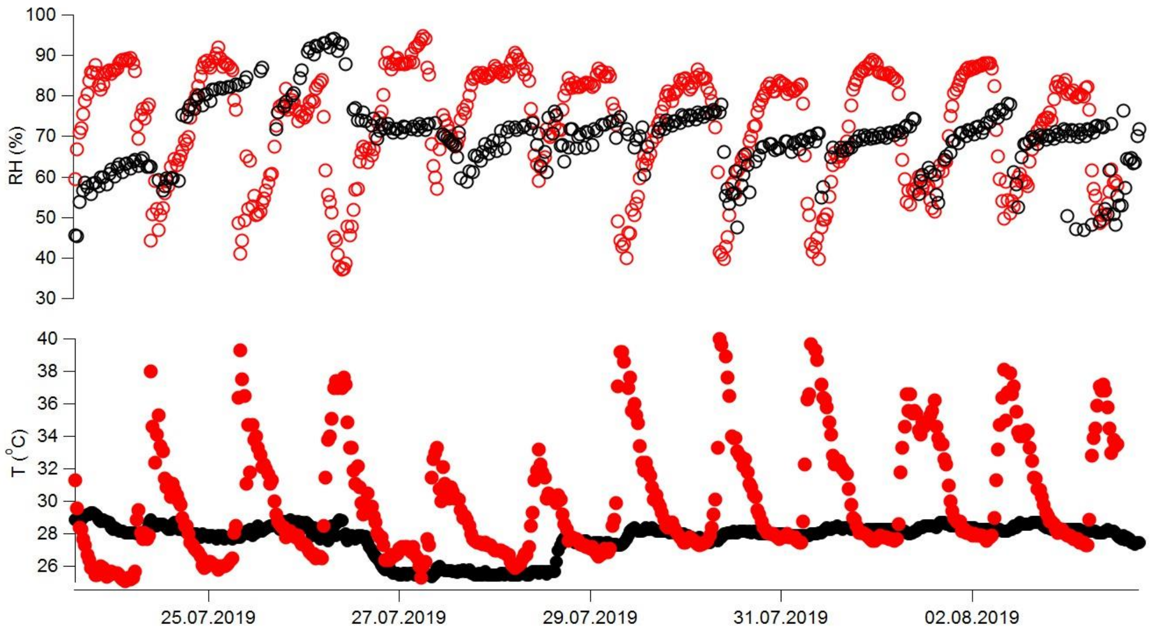

Figure S8: Time series of the half-hour averaged ambient RH (red open cycles in the upper panel) and temperature (red filled cycles in the lower panel) measurements in comparison to the reaction cell RH (black open cycles in the upper panel) and temperature (black filled cycles in the lower panel).

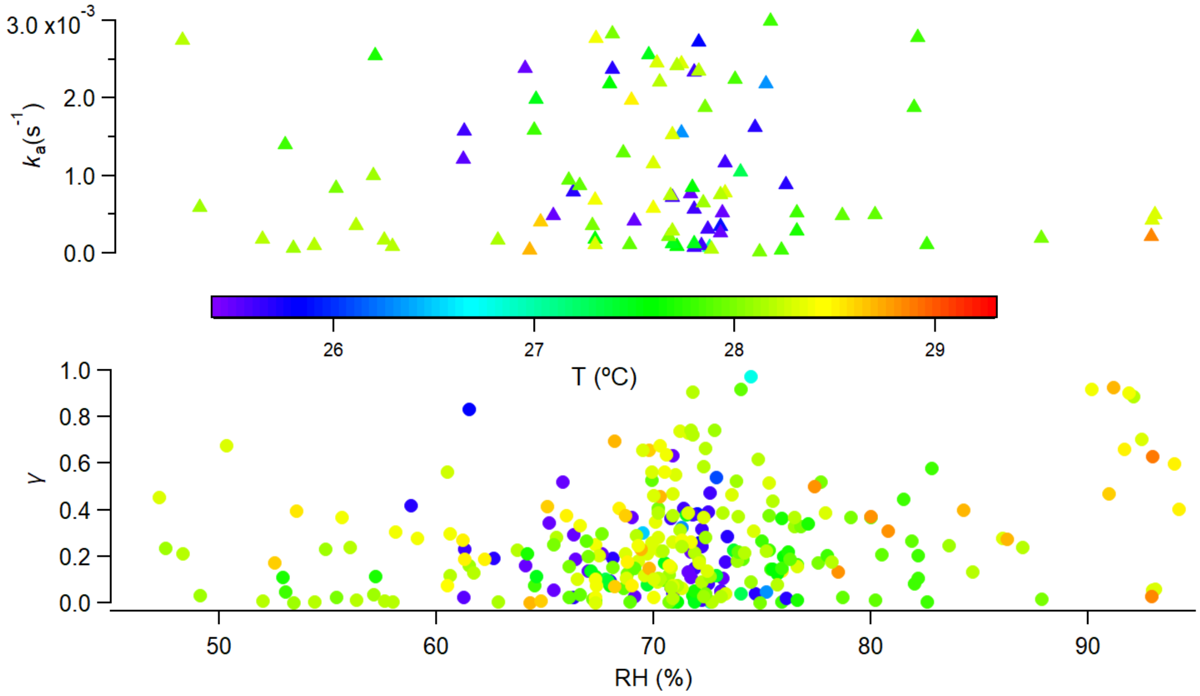

Figure S9: k_a and γ values as a function of RH in the reaction cell, colored coded with T.

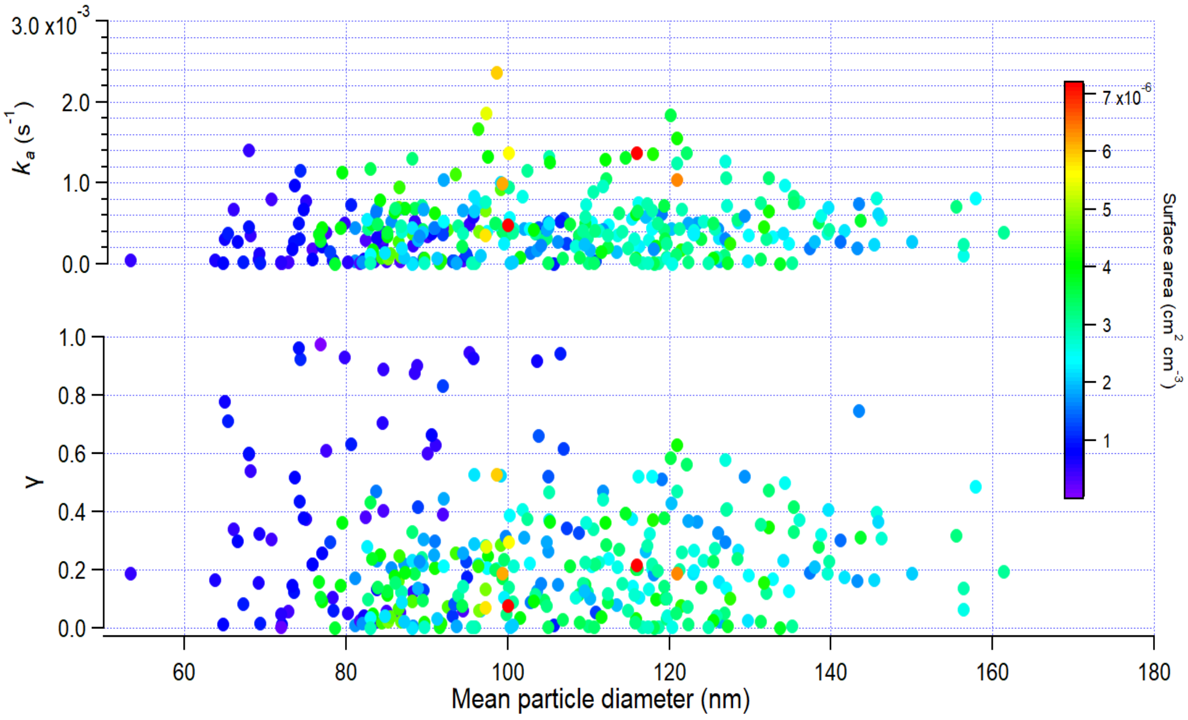

Figure S10: k_a (upper panel) and γ (lower panel) as a function of mean particle diameter, color coded with the surface area concentration.

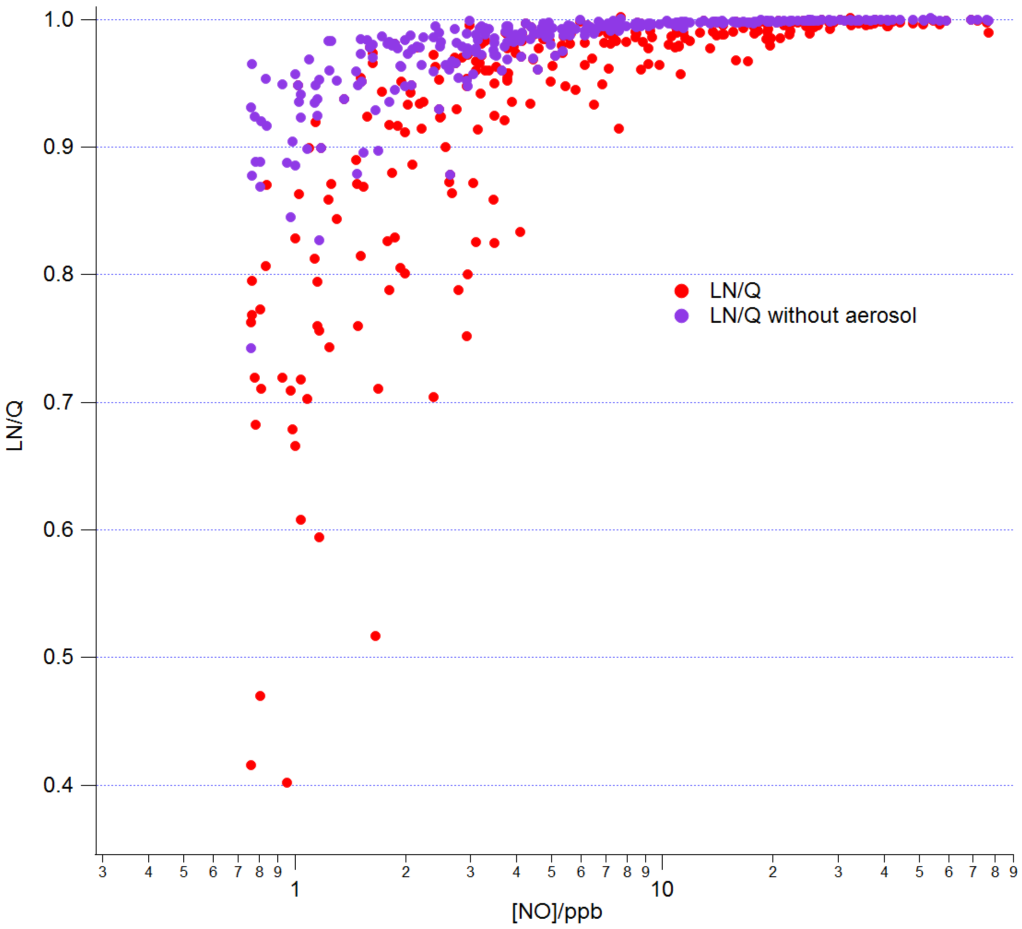

Figure S11: Dependence of day time LN/Q and LN/Q_without_aerosol on [NO].

Profiles of key factors used in Section 3.5:

Figure S12: Temporal variations in key factors in ambient air for determining XO_2 loss rates and $P(O_3)$ sensitivity in Sect. 3.6.

Table S1 Summary of equations and values used in Section 3.4.

Parameters	Equations and values	Ref.
ω/ cm s^{-1}	47376	
$\alpha^{\mathrm{HO_2}}*$	>0.2 (with copper (II)-doped aerosols)	[10-16]
H_{eff} /M atm^{-1}	$H_{\mathrm{HO_2}}(1+\frac{k_{eq}}{[H^+]})$	[17]
$H_{\mathrm{HO_2}}$/M atm^{-1}	EXP(4.9×4184/(8.314×T))	[18]
k_{eq}**	2.1×10^{-5}	[17]
$[H^+]$ /mol L^{-1}	10$^{-\mathrm{pH}}$	
pH	Calculated from the ISORROPIA-II model	
R /J mol^{-1} K^{-1}	8.314	
$[\mathrm{HO_{2(g)}}]$** *	1.0×10^{10}	[3]
r_p /cm	Measured by SMPS	
$k^{\mathrm{II}}_{\mathrm{TMI}}$ /M^{-1} s^{-1}	10^{9}	[17]
[TMI] /mol L^{-1} (using Cu^{2+} as surrogate) ****	$\frac{0.1\times[Cu]\ ***}{Liquid\ content\ in\ the\ aerosol\ ****}$	[19]
D_{aq}	10^{-5}	[17]

* Due to the aerosol particles collected in Yokohama City containing Cu, a high accommodation coefficient of HO$_2$ ($\alpha^{\mathrm{HO_2}}$) may lead to HO$_2$ uptake as an important sink of the HOx radical. According to the current research studies, we select $\alpha^{\mathrm{HO_2}}$ as 0.2 (typically for organics) and 0.5 (typically for inorganics) for the model simulation.

** HO$_2$ acid dissociation constant

***HO$_2$ concentration in the reaction cell, calculated using the same method as Zhou et al. (2019)[3].

**** Measured by off-line method

Table S2 Summary of equations and values used in Section 3.6.

Parameters	Equations and values	Ref.
k_a=$k_{\mathrm{HO_2}}$=$k_{\mathrm{RO_2}}$	Observed	
$k_{\mathrm{NO-XO_2}}$=$k_{\mathrm{NO-HO_2}}$=$k_{\mathrm{NO-RO_2}}$ /cm^3 molecule^{-1} s^{-1}	$3.3\times10^{12}\exp\left(\frac{270}{T}\right)$	[20]
[OH] /molecules cm^{-3}	10^6 (we assumed it is constant during the campaign)	
[$\mathrm{HO_2}$]* /molecules cm^{-3}	Day time (4:30 am – 7 pm): $\exp(8.4171\times10^{-13}[\mathrm{O_3}]+18.081)$ Night-time (7 pm – 4:30 am): $6.042\times10^{6}+1.841\times10^{-4}[\mathrm{O_3}]$	[21]
[$\mathrm{XO_2}$]/molecules cm^{-3}	[$\mathrm{HO_2}$] plus [$\mathrm{RO_2}$]	
[HCHO]**/ppb	2	
$k_{\mathrm{OH-VOCs}}$[VOCs]/s^{-1}	Total OH reactivity (k_{OH}*) minus $k_{\mathrm{OH+NO_2}}$[$\mathrm{NO_2}$]	
$k_{\mathrm{HO_2-HO_2}}$ /cm^3 molecule^{-1} s^{-1}	1.5×10^{-12}	[22]
$k_{\mathrm{HO_2-RO_2}}$ /cm^3 molecule^{-1} s^{-1}	$2.91\times10^{-13}\exp\left(\frac{1300}{T}\right)$ [1-exp(-0.245n)] (n = 4, assumed from observed VOCs distribution).	[23]
$k_{\mathrm{OH\text{-}HCHO}}$ /cm^3 molecule^{-1} s^{-1}	$8.2\times10^{-12}\times(T/298)\exp(0.33/(8.314\times T))$	[8]
$k_{\mathrm{OH-CO}}$ /cm^3 molecule^{-1} s^{-1}	2.4×10^{-13}	[20]
$k_{\mathrm{OH-NO_2}}$ /cm^3 molecule^{-1} s^{-1}	1.21×10^{-11}	[24]

*Measured in real time

**Average value measured during the campaign

References

1. Sadanaga, Y.; Yoshino, A.; Watanabe, K.; Yoshioka, A.; Wakazono, Y.; Kanaya, Y.; Kajii, Y., Development of a measurement system of OH reactivity in the atmosphere by using a laser-induced pump and probe technique. *Review of Scientific Instruments* **2004,** *75*, (8), 2648-2655.
2. Miyazaki, K.; Nakashima, Y.; Schoemaecker, C.; Fittschen, C.; Kajii, Y., Note: A laser-flash photolysis and laser-induced fluorescence detection technique for measuring total HO2 reactivity in ambient air. *Review of Scientific Instruments* **2013,** *84*, (7), 076106.
3. Zhou, J.; Murano, K.; Kohno, N.; Sakamoto, Y.; Kajii, Y., Real-time quantification of the total HO2 reactivity of ambient air and HO2 uptake kinetics onto ambient aerosols in Kyoto (Japan). *Atmospheric Environment* **2019**, 117189.
4. Sakamoto, Y.; Zhou, J.; Kohno, N.; Nakagawa, M.; Hirokawa, J.; Kajii, Y., Kinetics Study of OH Uptake onto Deliquesced NaCl Particles by Combining Laser Photolysis and Laser-Induced Fluorescence. *The Journal of Physical Chemistry Letters* **2018,** *9*, (14), 4115-4119.
5. Sioutas, C.; Kim, S.; Chang, M., Development and evaluation of a prototype ultrafine particle concentrator. *Journal of Aerosol Science* **1999,** *30*, (8), 1001-1017.
6. Matthews, P. S. J.; Baeza-Romero, M. T.; Whalley, L. K.; Heard, D. E., Uptake of HO₂ radicals onto Arizona test dust particles using an aerosol flow tube. *Atmos. Chem. Phys.* **2014,** *14*, (14), 7397-7408.
7. Brown, R. L., *Tubular flow reactors with first-order kinetics*. 1978; Vol. 83.
8. Sander, S. P., J. Abbatt, J. R. Barker, J. B. Burkholder, R. R. Friedl, D. M. Golden, R. E. Huie, C. E. Kolb, M. J. Kurylo, G.; K. Moortgat, V. L. O. a. P. H. W., Chemical Kinetics and Photochemical Data for Use in Atmospheric Studies, Evaluation No. 17. *Jet Propulsion Laboratory publication* **2011,** *JPL Publication 10-6*, (Jet Propulsion Laboratory, Pasadena, 2011 http://jpldataeval.jpl.nasa.gov.).
9. Chen, G.; Davis, D.; Crawford, J.; Hutterli, L. M.; Huey, L. G.; Slusher, D.; Mauldin, L.; Eisele, F.; Tanner, D.; Dibb, J.; Buhr, M.; McConnell, J.; Lefer, B.; Shetter, R.; Blake, D.; Song, C. H.; Lombardi, K.; Arnoldy, J., A reassessment of HOx South Pole chemistry based on observations recorded during ISCAT 2000. *Atmospheric Environment* **2004,** *38*, (32), 5451-5461.
10. Lakey, P. S. J.; George, I. J.; Baeza-Romero, M. T.; Whalley, L. K.; Heard, D. E., Organics Substantially Reduce HO_2 Uptake onto Aerosols Containing Transition Metal ions. *The Journal of Physical Chemistry A* **2016,** *120*, (9), 1421-1430.
11. Lakey, P. S. J.; Berkemeier, T.; Krapf, M.; Dommen, J.; Steimer, S. S.; Whalley, L. K.; Ingham, T.; Baeza-Romero, M. T.; Pöschl, U.; Shiraiwa, M.; Ammann, M.; Heard, D. E., The effect of viscosity and diffusion on the HO2 uptake by sucrose and secondary organic aerosol particles. *Atmos. Chem. Phys.* **2016,** *16*, (20), 13035-13047.
12. Taketani, F.; Kanaya, Y.; Akimoto, H., Kinetics of Heterogeneous Reactions of HO_2 Radical at Ambient Concentration Levels with $(NH_4)_2SO_4$ and NaCl Aerosol Particles. *The Journal of Physical Chemistry A* **2008,** *112*, (11), 2370-2377.
13. Thornton, J.; Abbatt, J. P. D., Measurements of HO_2 uptake to aqueous aerosol: Mass accommodation coefficients and net reactive loss. **2005,** *110*, (D8).
14. George, I. J.; Matthews, P. S. J.; Whalley, L. K.; Brooks, B.; Goddard, A.; Baeza-Romero, M. T.; Heard, D. E., Measurements of uptake coefficients for heterogeneous loss of HO2 onto submicron inorganic salt aerosols. *Physical Chemistry Chemical Physics* **2013,** *15*, (31), 12829-12845.
15. Taketani, F.; Kanaya, Y.; Akimoto, H., Heterogeneous loss of HO_2 by KCl, synthetic sea salt, and natural seawater aerosol particles. *Atmospheric Environment* **2009,** *43*, (9), 1660-1665.
16. Mozurkewich, M.; McMurry, P. H.; Gupta, A.; Calvert, J. G., Mass accommodation coefficient for HO_2 radicals on aqueous particles. **1987,** *92*, (D4), 4163-4170.
17. Thornton, J. A.; Jaeglé, L.; McNeill, V. F., Assessing known pathways for HO_2 loss in aqueous atmospheric aerosols: Regional and global impacts on tropospheric oxidants. *Journal of Geophysical Research: Atmospheres* **2008,** *113*, (D5).

18. Hanson, D. R.; Burkholder, J. B.; Howard, C. J.; Ravishankara, A. R., Measurement of hydroxyl and hydroperoxy radical uptake coefficients on water and sulfuric acid surfaces. *The Journal of Physical Chemistry* **1992,** *96*, (12), 4979-4985.

19. Ross, H. B.; Noone, K. J., A numerical investigation of the destruction of peroxy radical by Cu ion catalysed reactions on atmospheric particles. *Journal of Atmospheric Chemistry* **1991,** *12*, (2), 121-136.

20. Burkholder, J. B. S., S. P.; Abbatt, J.; Barker, J. R.; Huie, R. E.; Kolb, C. E.; Kurylo, 205 M. J.; Orkin, V. L.; Wilmouth, D. M.; Wine, P. H., Chemical Kinetics and photochemical Data for Use in Atmospheric Studies. *Evaluation No. 18. Jet Propulsion Laboratory: Pasadena, USA* **2015**, https://jpldataeval.jpl.nasa.gov/.

21. Kanaya, Y.; Cao, R.; Akimoto, H.; Fukuda, M.; Komazaki, Y.; Yokouchi, Y.; Koike, M.; Tanimoto, H.; Takegawa, N.; Kondo, Y., Urban photochemistry in central Tokyo: 1. Observed and modeled OH and HO2 radical concentrations during the winter and summer of 2004. *Journal of Geophysical Research: Atmospheres* **2007,** *112*, (D21).

22. Kanno, N.; Tonokura, K.; Tezaki, A.; Koshi, M., Nitrogen- and water-broadening coefficient measurements in the A˜2A′ ←X˜2A″ 000 − 000 band of HO2 using high-resolution diode laser two-tone frequency modulation spectroscopy. *Journal of Molecular Spectroscopy* **2005,** *229*, (2), 193-197.

23. Saunders, S. M.; Jenkin, M. E.; Derwent, R. G.; Pilling, M. J., Protocol for the development of the Master Chemical Mechanism, MCM v3 (Part A): tropospheric degradation of non-aromatic volatile organic compounds. *Atmospheric Chemistry and Physics* **2003,** *3*, (1), 161-180.

24. Sadanaga, Y.; Kondo, S.; Hashimoto, K.; Kajii, Y., Measurement of the rate coefficient for the $OH+NO_2$ reaction under the atmospheric pressure: Its humidity dependence. *Chemical Physics Letters* **2006,** *419*, (4), 474-478.